



Insights into the synergy effect of anisotropic {001} and {230} facets of BaTiO₃ nanocubes sensitized with CdSe quantum dots for photocatalytic water reduction

Donglin Zhong, Wenwen Liu, Pengfei Tan, Anquan Zhu, Yi Liu, Xiang Xiong, Jun Pan*

State key Laboratory of Powder Metallurgy, Central South University, Changsha, Hunan, 410083, China

ARTICLE INFO

Keyword:

CdSe quantum dots
BaTiO₃ nanocubes
Exposed crystal facet
Synergy effect
Photocatalytic water reduction

ABSTRACT

A novel kind of nanocomposites consisted of CdSe quantum dots (QDs) sensitized BaTiO₃ nanocubes was successfully synthesized by facile hydrothermal and chemical bath methods to investigate the synergy effect of isotropic {001} facets and anisotropic ({230} and {001}) facets on photocatalytic water reduction. The CdSe QDs were randomly decorated on the isotropic facets or anisotropic facets of BaTiO₃. The optimal CdSe QDs sensitization content was 7.5% (molar ratio), namely the 7.5% CdSe QDs sensitized BaTiO₃ composite showed significantly enhanced photocurrent response and photocatalytic performance. The superior photocatalytic activities of CdSe/BaTiO₃ composites were owing to the synergy effect of {001} and {230} facets including the charge separation and electronic reduction activities. The work suggested that crystal facet engineering had more promising application in the heterogeneous catalyst system.

1. Introduction

Photocatalytic hydrogen production from water splitting based on nano-semiconductor catalytic has attracted considerable attention and is considered to be an effective way to address the current energy shortage and environmental issues. [1–5] Generally speaking, the main factors affecting photocatalytic activity consists of the following three aspects: excitation of photogenerated carriers (include photogenerated electrons and holes), charge migration and separation as well as photocatalytic reaction on the catalytic surface. [2,6] To achieve maximum catalytic efficiency, rapid charge separation and efficient surface reactivity have attracted numerous research interest. [7–9] The recombination of photogenerated electron and hole pair is the essential cause of restraining the charge carriers possessed thermodynamically sufficient potentials for water splitting, which attributes to the absence of suitable reaction active sites. Hence, noble metals and non-noble metals can act as cocatalysts that provide active sites for surface catalytic reaction and improve the separation efficiency of charge. [10,11] On the other hand, doping of metal elements or non-metal elements and catalyst surface defects can serve as the trap of capturing the electrons or holes, so that the recombination of photogenerated electrons and holes can be reduced. [12,13] In addition, semiconductor-semiconductor junctions and crystal facet engineering have been developed to realize the separation of charge.

Recently, heterostructures have been investigated as a predominant strategy to enhance the separation of electron-hole pairs, such as hierarchical flower-like Ag₃PO₄/SnSe₂ composite, [14] g-C₃N₄/Ag₂CrO₄, [15] CuO_x/BiVO₄, [16] mesoporous WO₃/TiO₂ nanocomposites, [17] g-C₃N₄/TiO₂, [18] MoS₂ nanosheet@TiO₂ nanotube [19] and CeO₂/g-C₃N₄. [20] However, most of the studies reported only emphasized the coordination effect of composite structure and the function of band gap alignment impact in light absorption. On the other hand, investigations on crystal facet engineering of nano-semiconductors have indicated that photogenerated electrons and holes can transfer to disparate crystal facets, including BiVO₄, [21] TiO₂, [22,23] BiOBr, [24] SrTiO₃ [6] and ZnO [25]. Unfortunately, these studies only focus on spatial carrier separation itself result in semiconductor exposed different crystal facets, but seldom pay attention to the effect of crystal facet in multiphase semiconductor composite structure. In the study of crystal facet engineering, our previous study by Liu et al. investigated spatial carrier separation and photocatalytic performance of doped BiOCl, illuminating that iodine doping is a novel strategy to improve the spatial carrier separation of BiOCl nanoplates. [26] However, it is ambiguous why the exposure of various facets can lead to a very different activity in the composite structure of multiphase semiconductor, especially the synergy effect of different exposed facets seem to be concerned in the heterogeneous catalyst system.

In this report, to address above unclear issue, cubic phase BaTiO₃

* Corresponding author.

E-mail address: jun.pan@csu.edu.cn (J. Pan).

Table 1The denomination of the prepared CdSe/BaTiO₃ composites.

Sample	BTO-L-5	BTO-L-7.5	BTO-L-10	BTO-H-5	BTO-H-7.5	BTO-H-10
BTO-H ^a	–	–	–	2 mmol	2 mmol	2 mmol
BTO-L ^b	2 mmol	2 mmol	2 mmol	–	–	–
CdAc ₂ ·2H ₂ O	0.1 mmol	0.15 mmol	0.2 mmol	0.1 mmol	0.15 mmol	0.2 mmol
Time	10 min	15 min	20 min	10 min	15 min	20 min

^a BaTiO₃ enclosed with anisotropic {230} and {001} crystal facets.^b BaTiO₃ only enclosed with isotropic {001} crystal facets.

nanocubes supported CdSe QDs composite is believed to be a suitable model. Taking into consideration to the stability, resistance to photo-corrosion and matching conduction band potentials for water splitting, BaTiO₃ may be a suitable candidate for the catalyst. Moreover, cubic phase BaTiO₃ can be easily adjusted morphology to exposed isotropic facets and anisotropic facets. However, 3.2 eV of band gap and only ultraviolet response severely limit the application of BaTiO₃. The tunable band gap of CdSe QDs (1.8–3.0 eV) can simply solve the problem of visible light response and light absorption. Nevertheless, serious photocorrosion and high possibility of photogenerated carrier recombination similarly inhibit CdSe photocatalytic efficiency. To expound the essential mechanism of improving the photocatalytic efficiency, CdSe QDs were randomly distributed on isotropic facets ({001}, 6-facet BaTiO₃) and anisotropic facets ({001} and {230}, 30-facet BaTiO₃). Interestingly, we observed that CdSe QDs deposited on 30-facet BaTiO₃ revealed superior performance compared to CdSe QDs sensitized 6-facet BaTiO₃. Furthermore, the result of photoelectrochemical measurements were found the consistent verdicts. The high-efficiency photocatalytic activity can owe to the high efficiency of charge separation between CdSe QDs and BaTiO₃ and synergy effect of {001} and {230} facets on reducing the recombination of photogenerated charges.

2. Experimental section

2.1. Preparation of BaTiO₃

BaTiO₃ enclosed with different crystal facets was prepared by the simple one-pot solvothermal method with minor modification of the procedure reported by Wang et al. [27] In a typical synthesis, tetrabutyl titanate (2.5 mmol) was slowly dropped in ethanolamine (EA, 5 mL) under stirring at room temperature. Then, NaOH (4.8 M, 12.5 mL) and BaCl₂·2H₂O (1.0 M, 2.5 mL) was added dropwise to the mixture in turn to form a white precipitate suspension. Subsequently, the obtained suspension solution was then sealed in a 50 mL Teflon-lined stainless steel autoclave and hatched at 180 °C for 24 h. After natural cooling, the reaction white precipitates were centrifuged and washed with ethanol and deionized water repeatedly to remove the residual reactants, and dried at 60 °C in an vacuum oven.

For comparison, BaTiO₃ only enclosed with isotropic {001} facets was synthesized by tuning the concentrations of NaOH (4.8 M–14.4 M) and EA (5 mL–10 mL), followed by heat treatment at 200 °C for 24 h. The BaTiO₃ enclosed with anisotropic {230} and {001} crystal facets and that only enclosed with isotropic {001} facets were named as BTO-H and BTO-L, respectively.

2.2. Preparation of CdSe QDs

The CdSe QDs were synthesized by imitating previous reported work. [28] In a typical routine utilizing a three-neck flask, in order to prepare the Se precursor, Na₂SO₃ (0.03 mol) and selenium powder (5.0 mmol) were added into 100 mL deionized water and refluxed under a nitrogen atmosphere at 80 °C for 6 h. After that, CdAc₂·2H₂O (4 mmol) was dissolved in 50 mL of deionized water and then 100 mL Se precursor was added dropwise into the mixture at 500 µL/min using

a peristaltic pump during reflux and insulation at 80 °C for 6 h. The crimson precipitates were centrifuged and washed with ethanol and deionized water repeatedly to remove the residual reactants, and dried at 60 °C in an vacuum oven, labeled as CS.

2.3. Sensitization of CdSe QDs on BaTiO₃

In a typical decoration process, the above BaTiO₃ product (2 mmol), various amount CdAc₂·2H₂O and L-cysteine (2 mmol) were dissolved in 25 mL deionized water. After stirring 1 h, the above solution was refluxed and maintained at 80 °C, Se precursor was added dropwise into the solution at 500 µL/min for different time, corresponding to different amount Cd resource, respectively. The final products were quenched in ice water and washed, denoting as the following table (Table 1).

2.4. Photocatalytic tests

The photocatalytic performance of various photocatalysts were assessed using water reduction by the irradiation of a Xe lamp (300 mW cm^{−2}) under the visible light ($\lambda \geq 420$ nm) derived from a 420 nm cut-off filter. In a typical photocatalytic hydrogen evolution reaction, 20 mg of as-prepared catalyst powder was added into 100 mL of 0.05 M Na₂SO₃ and 0.05 M Na₂S mixed aqueous solution. The suspension solution was irradiated by 300 W Xe lamp with reaction temperature maintained at 10 °C by circulation condensate. The H₂ gas was produced and determined once per hour using a top-irradiation type Pyrex cylindrical reactor attached to a closed glass gas system.

2.5. Electrochemical analysis

The relevant photoelectrochemistry measurements, including the transient state photocurrent response and electrochemical impedance spectra (EIS) of as-prepared catalyst, were examined by a CHI 660e electrochemical work station. Typically, indium tin oxide (ITO) glass (1 cm × 1 cm) was utilized to prepare working electrodes via drop-casting the catalyst slurry that was obtained through dispersing photocatalyst (20 mg) in the mixed solution (2 mL) of ethylene glycol (1.5 mL) and deionized water (0.5 mL) with 50 µL of Nafion. After evaporation of the solvent, the electrode was heat treatment at 280 °C for 2 h under vacuum so that the compact combination between photocatalyst thin film and ITO surface could be formed. The photocurrent-time and EIS curves were separately recorded at the applied potential of 0.4 eV and 1.5 eV using a standard three-electrode system, in which a saturated Ag/AgCl electrode, platinum foil and Na₂SO₄ (0.5 M) aqueous solution were acted as the reference electrode, counter electrode and electrolyte, respectively. Mott-Schottky measurements were recorded at a constant frequency of 1000 Hz with 10 mV amplitude at applied potentials from −1.0 V to 1.0 V under the dark condition.

3. Results and discussion

X-ray diffraction (XRD) was performed to analyze the composition phase structure and crystallography of our experimental products

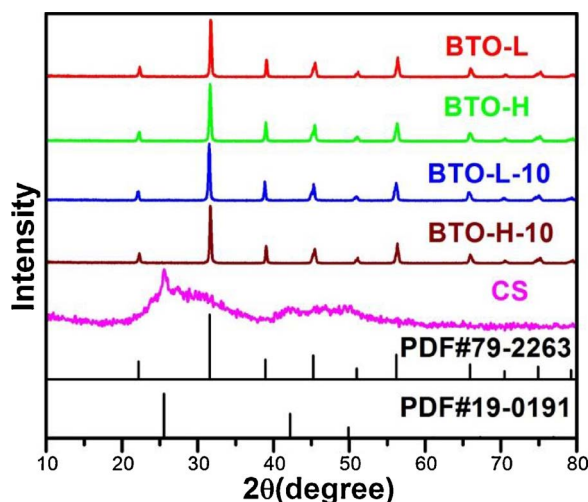


Fig. 1. XRD patterns of BTO-L, BTO-H, BTO-L-10, BTO-H-10 and CS.

(Fig. 1). XRD patterns of bare BTO-H and BTO-L readily index to the cubic structure of BaTiO_3 with the characteristic peaks situated at 31.558° , 45.233° and 56.197° , corresponding to the (110), (200) and (211) planes of cubic-phase BaTiO_3 (JCPDS No. 79-2263). XRD pattern of pure CdSe QDs confirms the cubic phase of CdSe with three diffraction peaks located at 25.354° , 42.008° and 49.698° , corresponding to the (111), (220) and (311) planes of cubic-phase CdSe, respectively (JCPDS No. 19-0191). For the CdSe/ BaTiO_3 compound sample, no other peaks appear except that of BaTiO_3 , owing to the amount of CdSe was too low to be detected by XRD measurement. According to these results, BaTiO_3 and CdSe were successfully prepared.

In order to further prove the presence of CdSe in the as-prepared composite samples, X-ray photoelectron spectroscopy (XPS) measurements were employed to directly investigate the chemical compositions and charge states of CdSe QDs and BaTiO_3 (Fig. 2). Fig. 2a shows the XPS full spectrum of BTO-L-7.5 composite sample, from which all peaks can be seen to ascribe to Ba, Ti, O, Cd, Se and C elements for the CdSe sensitized BaTiO_3 . From Fig. 2b–d, the peaks of Ba $3d_{5/2}$, Ba $3d_{3/2}$, Ti $2p_{3/2}$, Ti $2p_{1/2}$ and O 1s are centered at 778.6 eV, 794.2 eV, 458.1 eV, 464.2 and 529.4 eV, respectively, which distinctly correspond to the characteristic values of BaTiO_3 . [2] The binding energies of Cd $3d_{5/2}$, Cd $3d_{3/2}$ and Se 3d appeared at 405.0 eV, 411.7 eV and 54.0 eV, which are in agreement with the typical values of CdSe reported by previous literature. [29]

In order to obtain the chemical information of bonding structure in the as-synthesized samples, the homologous Fourier transform infrared spectra (FT-IR) of CS, BTO-L-7.5 and BTO-L were detected and shown in Fig. 3. In terms of the original BTO-L and CS, the broad absorption peaks present at 3441 cm^{-1} and 3448 cm^{-1} that both derive from O–H stretching, suggesting the existence of infinite amounts of H_2O and OH^- in the samples. [30,31] The peaks appeared at 1628 cm^{-1} and 1629 cm^{-1} are corresponding to C=O stretching vibrations for pure CdSe and BaTiO_3 samples. The C=O stretching vibration were detected, indicating the presence of acetate ions adsorbed on the surface of samples. Based on FT-IR spectra result, it indicates that the surface state of CdSe quantum dots (QDs) sensitized BaTiO_3 composite has the common surface characteristic of pure CdSe and BaTiO_3 .

As shown in Fig. 4, the surface morphologies of these different morphologies BaTiO_3 samples with various crystal facets were detected by the field-emission scanning electron microscope (FE-SEM). From Fig. 4a–f, it is found that the BaTiO_3 are approximately uniform cubes, and their size distribution vary from 200 nm to 300 nm. Interestingly, compared with the 6-facet BTO-L exposed isotropic facets {001}, the BTO-H sample exhibits anisotropic facets that build a 30-facet BaTiO_3 nanocube. Fig. 4b shows the unambiguous the transmission electron

microscopy (TEM) image of near-perfect cubic BaTiO_3 , while a inerratic 12 edges of projection is observed from Fig. 4e. The schematic descriptions of different morphologies of BaTiO_3 nanocrystals, 6-facet and 30-facet nanocubes, are clearly depicted as Fig. 4c and f, respectively.

To obtain the deep information of corners, edges and exposed facets of the as-synthesized BaTiO_3 nanocrystals, we display the typical TEM, high-resolution TEM (HR-TEM) images and the corresponding selected area electron diffraction (SAED) patterns in Fig. 5. The primary contrast difference between the cube vertex parts of different morphologies BaTiO_3 nanocrystals indicates the sharp corner blunts to two flat surfaces at the edges of BaTiO_3 nanocubes, which is due to the introduction of other crystal surfaces. The isotropic crystal facets nature of the single-crystalline BTO-L was indicated by the diffraction pattern of bright intense spots in Fig. 5b, suggesting the 6 nondiscriminatory facets of cubic BaTiO_3 should be uniform {001}. The HR-TEM images (Fig. 5c) was measured from {001} facet, indicating two sets of lattice fringes with the same spacing of 0.176 nm and the fringes angle of 90° , which are respectively corresponded to the (–110) and (110) planes of cubic phase BaTiO_3 . Thus, we draw the conclusion that the top facet of the nanocrystal in Fig. 5a can be confirmed as the (001) facet, which is consistent with previous characterization results. According to Steno's law, it's believed that the included angle between the corresponding crystal facets should have fixed corresponding relation. Therefore, we magnified Fig. 5d broken circle area (I) and got the detailed information of included angles. It is divided into two groups, one is 146.9° and the other is 157.0° . Based on the equation of included angle for a cubic system:

$$\cos\theta = \frac{h_1h_2 + k_1k_2 + l_1l_2}{\sqrt{h_1^2 + k_1^2 + l_1^2}\sqrt{h_2^2 + k_2^2 + l_2^2}} \quad (1)$$

the exposed facets are able to calculate and determine as (–230) and (2–30), respectively, both of them belong to {230} crystal plane. Fig. 5f is the HR-TEM image of broken circle area (II), revealing the same lattice fringes as (110) facet. As a consequence, the top view is still defined as (001) facet.

The 3D projection image of cubic BaTiO_3 nanocrystals is shown in Fig. 6a. The exposed anisotropic facet of 30-facet BaTiO_3 is the {230} and {001} facets both with O and Ba atoms on the surface (Fig. 6b and c), while the atomic arrangement and distance are different between anisotropic{230} and {001} facets. From Fig. 6c, in terms of the exposed isotropic facet of 6-facet BaTiO_3 , the exposed facet is identical {001} facet. Therefore, it is difficult to realize the synergy effect of specific facets for photocatalytic reaction. To reach this aim, the exposed facet of BaTiO_3 nanocubes is rationally adjusted from isotropic facets to anisotropic facets.

CdSe QDs sensitized BaTiO_3 nanocubes composite structure were investigated by magnified TEM and HR-TEM pattern, as shown in Fig. 7. The standard TEM images clearly indicate the presence of CdSe QDs, which randomly distribute on {001} and {230} facets in Fig. 7a and d. From the further enlarge HR-TEM images Fig. 7c and e, we can clearly observe that the diameter sizes of CdSe QDs distribute between 5 nm and 10 nm. The lattice fringe gained from the representative CdSe QDs suggests the distance between two consecutive planes (Fig. 7c and f). The lattice fringe spacing of 0.2728 nm is corresponded to the theoretical value of cubic phase CdSe (311) crystal plane, conforming to the XRD result.

The optical property was examined via UV–vis absorption spectrum. As illustrated in Fig. 8, the light absorption ability and band gaps of BTO-L and BTO-H are approximately equal. This result indicate that the difference of photocatalytic activity between BTO-L-7.5 and BTO-H-7.5 should not be caused by the light absorption characteristics of various morphologies BaTiO_3 . In other word, the differences in morphology have little effect on the band gaps of the BaTiO_3 samples. In order to further eliminate the influence of surface area for photocatalytic property, the surface areas of as-synthesized BaTiO_3 samples were

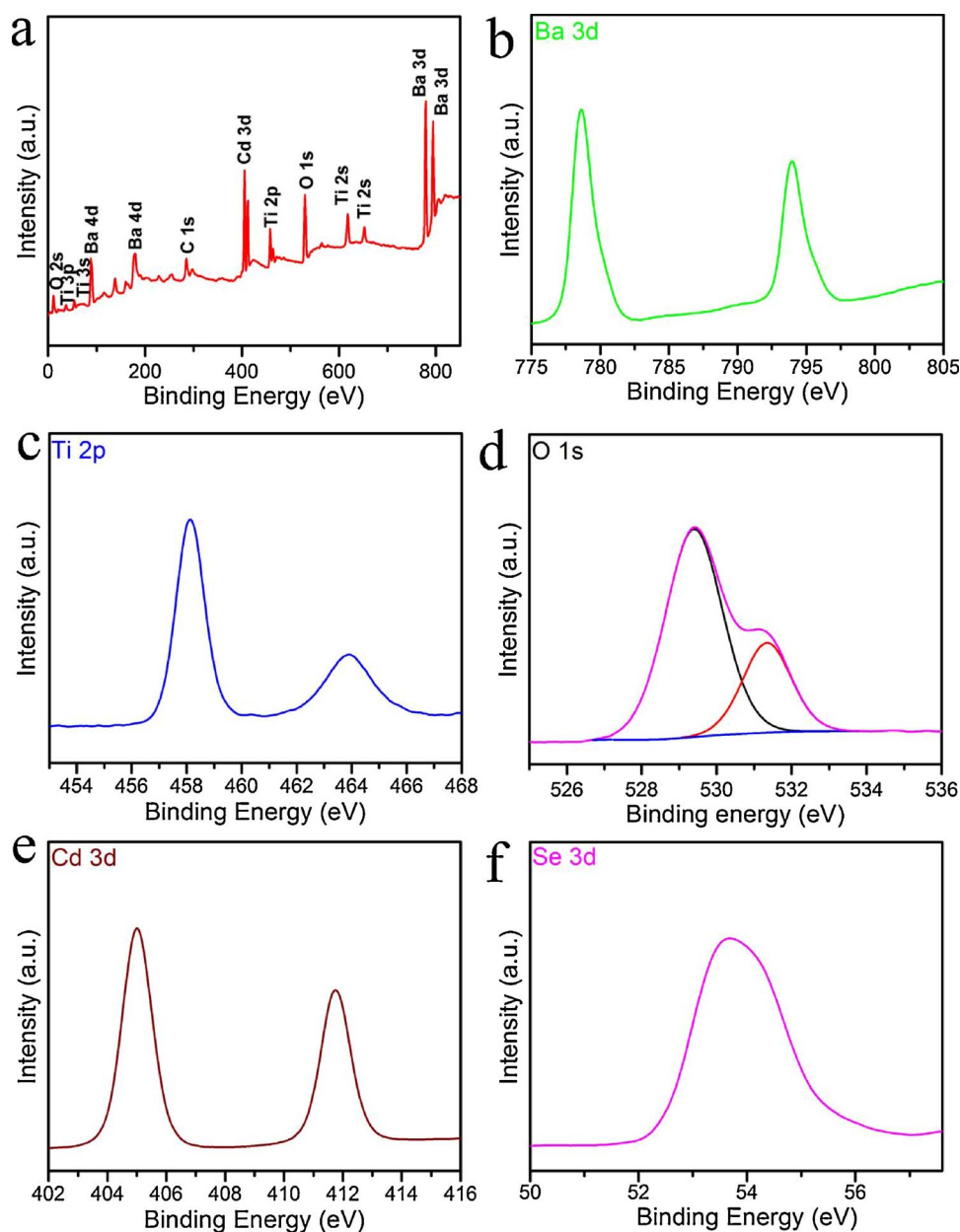


Fig. 2. (a) X-ray photoelectron spectra of BTO-L-7.5. (b) Ba 3d, (c) Ti 2p and (d) O 1s XPS of BTO-L. (e) Cd 3d and (f) Se 3d XPS of CdSe.

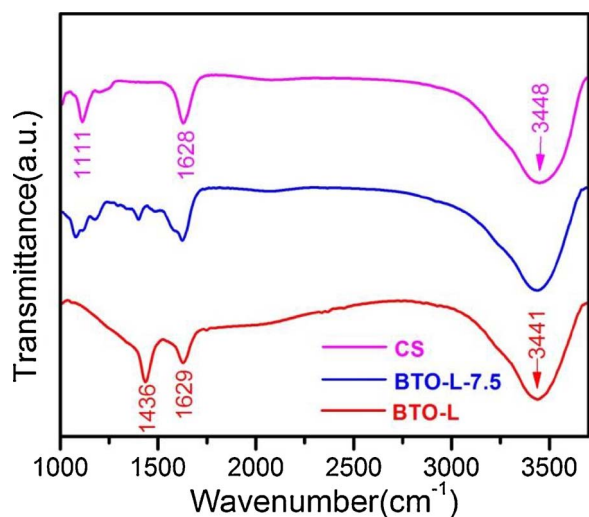


Fig. 3. FT-IR spectra of CS, BTO-L and BTO-L-7.5.

evaluated and shown in Table 2. The BET surface areas of these samples have no remarkable distinction, illuminating that the difference of photocatalytic activities should not be caused by surface area.

Generally, the photocatalyst with exposed different surfaces, including the isotropic facets and anisotropic facets, which shows more superior photocatalytic performance attributed to spatial separation of photogenerated carriers. [32,33] However, little attention has been paid to the effect of isotropic facets and anisotropic facets on photogenerated carriers separation in the heterogeneous catalysts system. To better comprehend the mechanism and path of carriers transfer, photocatalytic performance of CdSe QDs sensitized BaTiO₃ that enclosed with various facets were measured under visible light radiation (Fig. 9). As shown in Fig. 9a, the photocatalytic hydrogen evolution activity is consumingly dependent on the hybrid amount of CdSe QDs. In the case of BTO-L-X (X = 5, 7.5 or 10), the highest photocatalytic water reduction activity is achieved for the BTO-L-7.5 sample with loading 7.5% CdSe QDs on the surface of BaTiO₃. There is a point should be noted that CdSe QDs play a role as electron donors and BaTiO₃ act as electron acceptors, respectively, so that the photogenerated electrons worked for

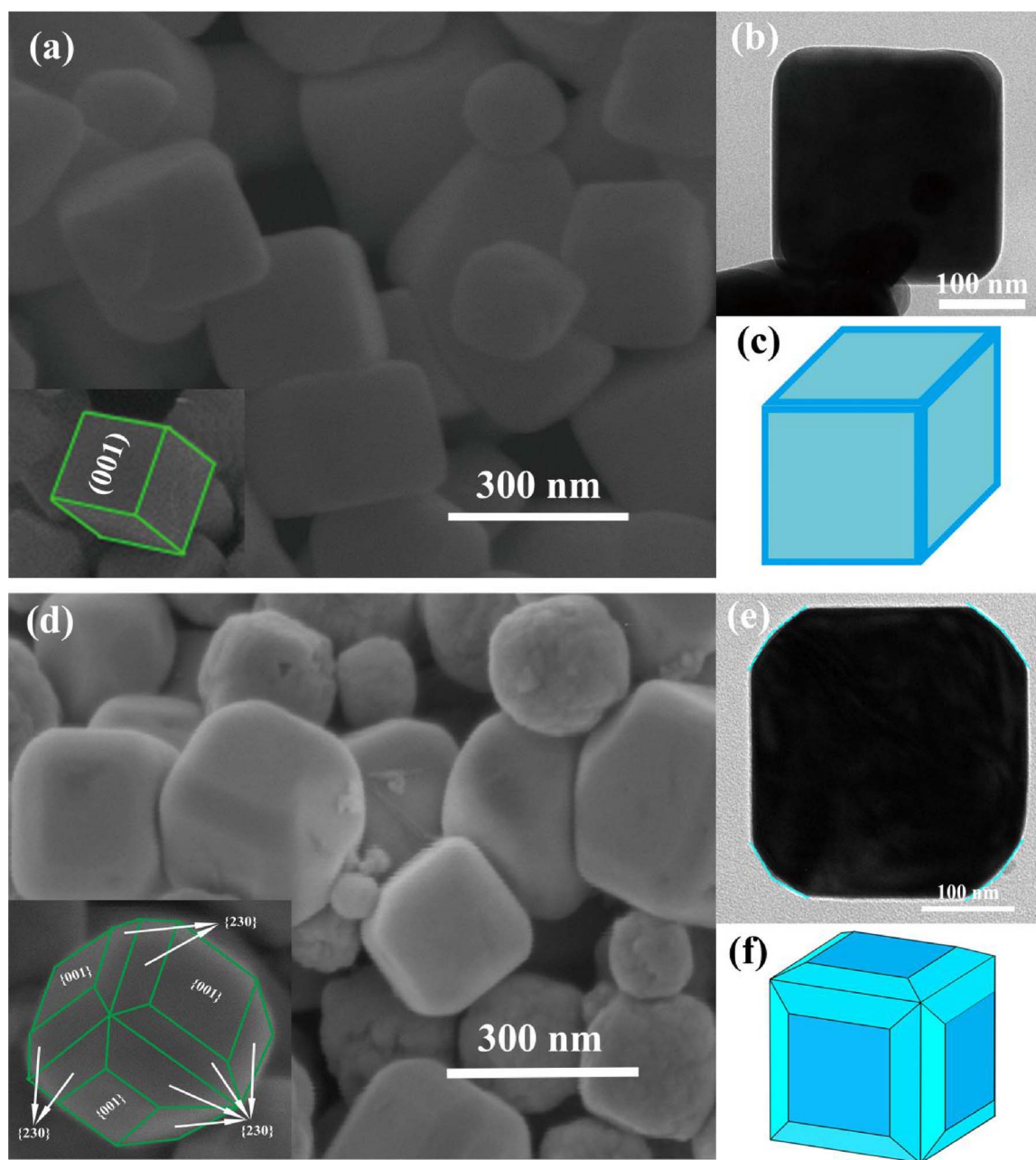


Fig. 4. Magnified FE-SEM images, TEM images, and schematics of respective BaTiO_3 cubes are shown with different facets named as BTO-L (a–c) and BTO-H (d–f).

photocatalytic reduction reaction need to transfer from external CdSe to internal BaTiO_3 . In other words, if the content of CdSe is too low to provide sufficient number of active sites and electrons, but too high will lead to the surfaces of the BaTiO_3 are covered and CdSe QDs aggregation and growth which prevent water molecules contacting with the active site. It is verified by the result of the experiment, when the content of CdSe increases from 5% to 7.5%, the photocatalytic performance can be most greatly enhanced. However, the content of CdSe is further improved to 10%, the photocatalytic activity is suppressed by a certain degree. For comparison, the photocatalytic water splitting hydrogen production of BTO-H-7.5 was performed. It turns out that when the anisotropic functional facets exist, namely the 7.5% CdSe QDs are randomly dispersed on the isotropic/anisotropic facets of BaTiO_3 , the photocatalytic activity can be comparatively enhanced.

The result indicates that the greatest improvement on photocatalytic hydrogen evolution activity is achieved for the BTO-H-7.5 sample enclosed with {001} and {230} facets. On the basis of our

previous experiment and Pan's report, [20] we draw a conclusion that {001} and {230} facets are both functionalized for the photocatalytic reduction reaction, while the exposure of anisotropic {230} facets gives rise to superior photocatalytic activity. Therefore, we assume that {001} and {230} facets maintain the effect after forming heterogeneous catalysts by CdSe QDs sensitization so that could still accelerate charge separation from CdSe QDs to the functional facets for photo-reduction reaction, which ensures the maximized photocatalytic activity achieved over the surface-reconstructed hybrid samples enclosed with reduction-functionalized {001}/{230} facets. Moreover, as is known to all, the presence of various facets can adjust the potential of Fermi level, which will change the potential barrier of electrons transfer from electron donor to the receptor to some extent and cause the difference of electrons reduction activity. To compare the intrinsic activities of catalysts, Turnover Frequency (TOF) was generally estimated. In the heterogeneous structure without a noble-metal cocatalyst, the combination interface of the two phase frequently plays the role of active site. [34]

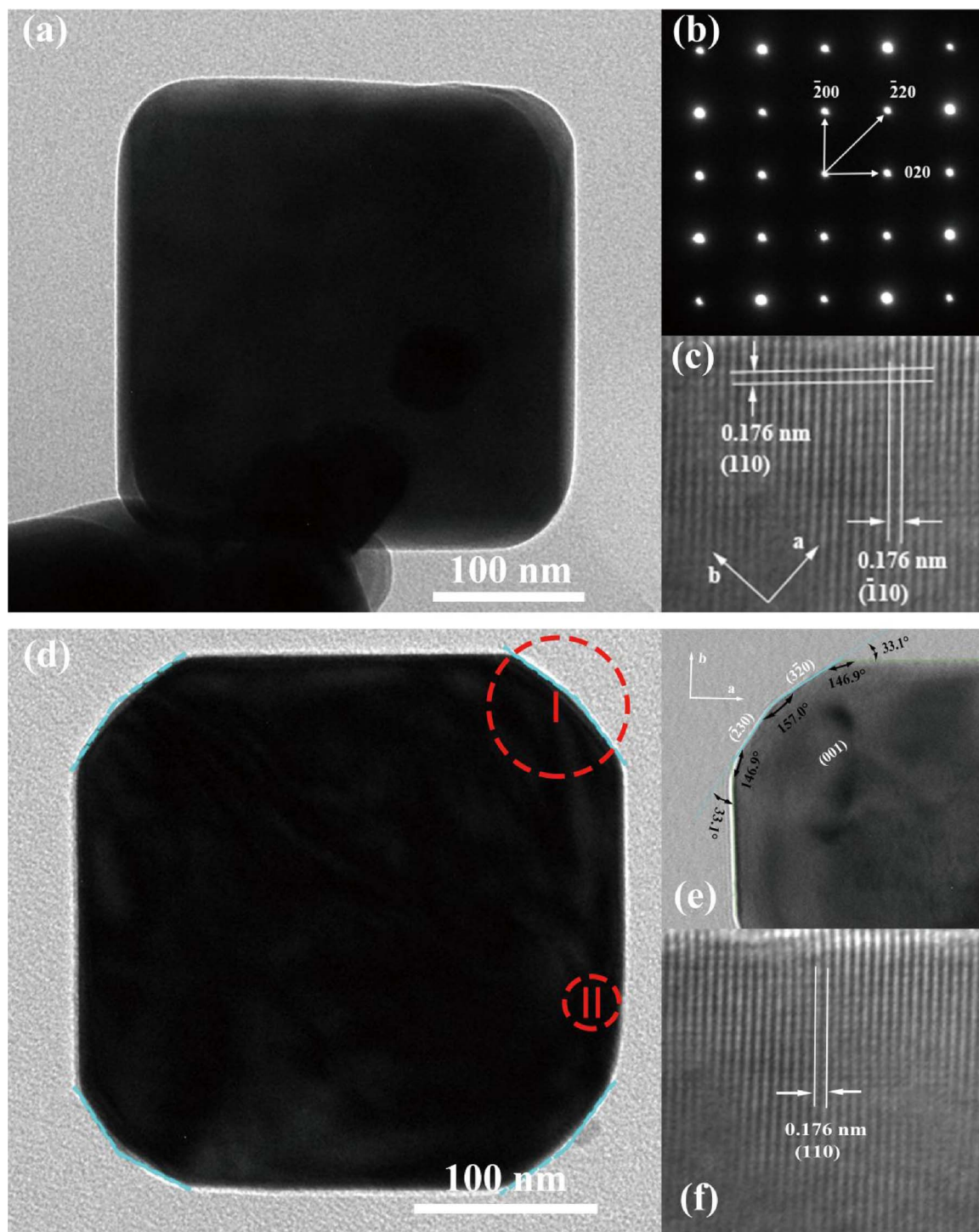


Fig. 5. Typical TEM images, HR-TEM images, and SAED pattern of respective BaTiO₃ cubes are shown with different facets named as BTO-L (a–c) and BTO-H (d–f).

In other word, the unusual photocatalytic activity arises from the positive synergetic effect between the CdSe and BaTiO₃ components in this hybrid structure, in which CdSe can act as a source of active adsorption sites. Hence, the content of cadmium atom is mass approximation for the number of active site. To determine the number of active site, atomic absorption spectrometry (Atomic absorption spectrophotometer, TAS-990 super) was carried out to detect the molar quantities of cadmium atom. According to the test results, the content of cadmium atom are 3.29% and 3.03% for BTO-L-7.5 and BTO-H-7.5, respectively. Then, TOF were calculated according to Eq. (2) [35–37]

$$\text{TOF}(h^{-1}) = \frac{A \times M(\text{Me}) \times 10^{-3}}{X(\text{Me}) \times D} \quad (2)$$

where A ($\text{mmol}_{\text{H}_2} \text{g}_{\text{Catal}}^{-1} \text{h}^{-1}$) is the rate of Hydrogen production, M (Me) (g mol^{-1}) is the molar mass of the supported metal, $X(\text{Me})$ (%) is the metal content in the catalyst and D is the total amount of the catalyst. TOF of 1.117 h^{-1} and 1.981 h^{-1} are obtained for BTO-L-7.5 and BTO-H-7.5, respectively. (Table 2) Therefore, the significant enhancement in photocatalytic performance for BTO-H-7.5 sample should be reasonably attributed to the enhanced charge transfer, separation and photocatalytic activity caused by the anisotropic reductive facets

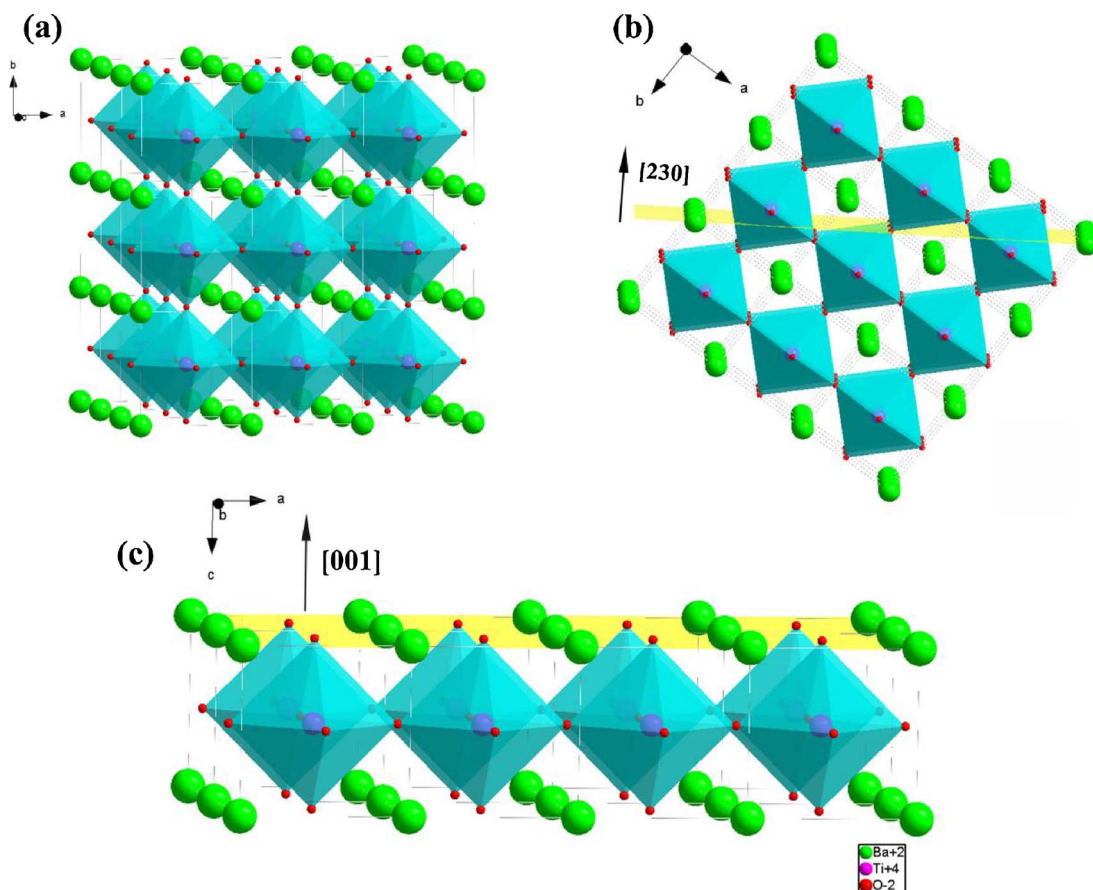


Fig. 6. (a) 3D projection of the BaTiO₃ of perovskite structure (b) The structure of the {230} facet of BaTiO₃. (c) The structure of the {001} facet of BaTiO₃.

introduced into the surface of BTO-L. On the other hand, from the recycle experiments of BTO-H-7.5 sample presented in Fig. 9b, the stability of photocatalytic hydrogen production can maintain very well after four cycles. It indicates that the composite structure of CdSe QDs sensitized BaTiO₃ possesses a stable structure.

In general, the catalyst selectively enclosed with isotropic and anisotropic facets that have different surface structural configuration shows diverse effects on photo-oxidation or photo-reduction activity, respectively. [19,22] This phenomenon is generally attributed to higher efficiency of photogenerated electron-hole pairs separation or inhibition of the photogenerated charges recombination. In addition, on account of the light absorption ability and surface area are not the defining factors that affect photocatalytic performance, photoelectrochemical (PEC) properties of the as-prepared samples were evaluated to identify whether the efficiencies of photogenerated charge transfer and separation were the dominant factors in governing the photocatalytic performance of CdSe QDs sensitized BaTiO₃ composite (Fig. 10). To confirm this hypothesis, the transient photocurrent responses were assessed by applying a 0.4 V potential to the electrodes in cyclic 20 s intervals. In Fig. 10a, the photocurrent densities for all samples are seen to be low under non-illumination, illustrating there is no presence of photoexcited electrons and holes. When the electrodes are illuminated under visible light, the photocurrent responses in all samples enhance due to the excitation occurring of charge carriers. In terms of the original BaTiO₃ electrodes, the photoanode current of BTO-H is obviously more increased than that of BTO-L. Hence, the improved photocurrent responses in BTO-H demonstrates that the charge transfer efficiency and light utilization can be improved by exposing {230} functional facets in BaTiO₃. The current density of pure CdSe QDs in Fig. 5a is slightly enhanced, which originates from the narrower band gap and more prominent ability of light absorption. On the other hand,

for the CdSe QDs sensitized BaTiO₃ hybrid structure, a comparatively higher photocurrent response with stronger photocurrent intensity can be observed. Moreover, compared with BTO-L-7.5, a much stronger photocurrent response with distinctly boosted photocurrent intensity can be observed from the BTO-H-7.5. This observation indicates that the occurrence of a more substantially efficient photoexcited electron and hole pairs separation in our BTO-H-7.5 sample. In order to further validate the charge transfer process of the as-synthesized sample, electrochemical impedance spectra (EIS) analysis was carried out and the investigation result were presented in Fig. 10b. From the EIS Nyquist plots, the arc radius of BTO-L is obviously longer than that of BTO-H, while the bare CdSe QDs sample shows a smaller arc radius compared to both of them. Additionally, the smaller arc can be observed from BTO-H-7.5 compared with BTO-L-7.5, revealing that the presence of anisotropic {230} facets leads to a lower charge transfer resistance resulted from the more effective separation of carriers. Accordingly, transient photocurrent responses and these EIS results conclusively verify that, compared to the BTO-L-7.5 of only containing isotropic {001} facets, the BTO-H-7.5 enclosed with isotropic/anisotropic {001}/{230} facets can facilitate a more efficient charge separation of photogenerated electrons and holes and lead to the boosted photocatalytic activity.

In order to more profoundly understand the photocatalytic mechanism and charge transfer process, the optical properties and band structures of as-synthesized materials were studied (Fig. 11). According to the previous UV-vis DRS of the as-synthesized BTO-L, BTO-H and CS samples (Fig. 8), the corresponding band gap energies (E_g) were acquired via the Kubelka-Munk equation: [8]

$$\alpha h\nu = A(h\nu - E_g)^n \quad (3)$$

where α , h , ν , E_g and A are absorption coefficient, Planck constant, light

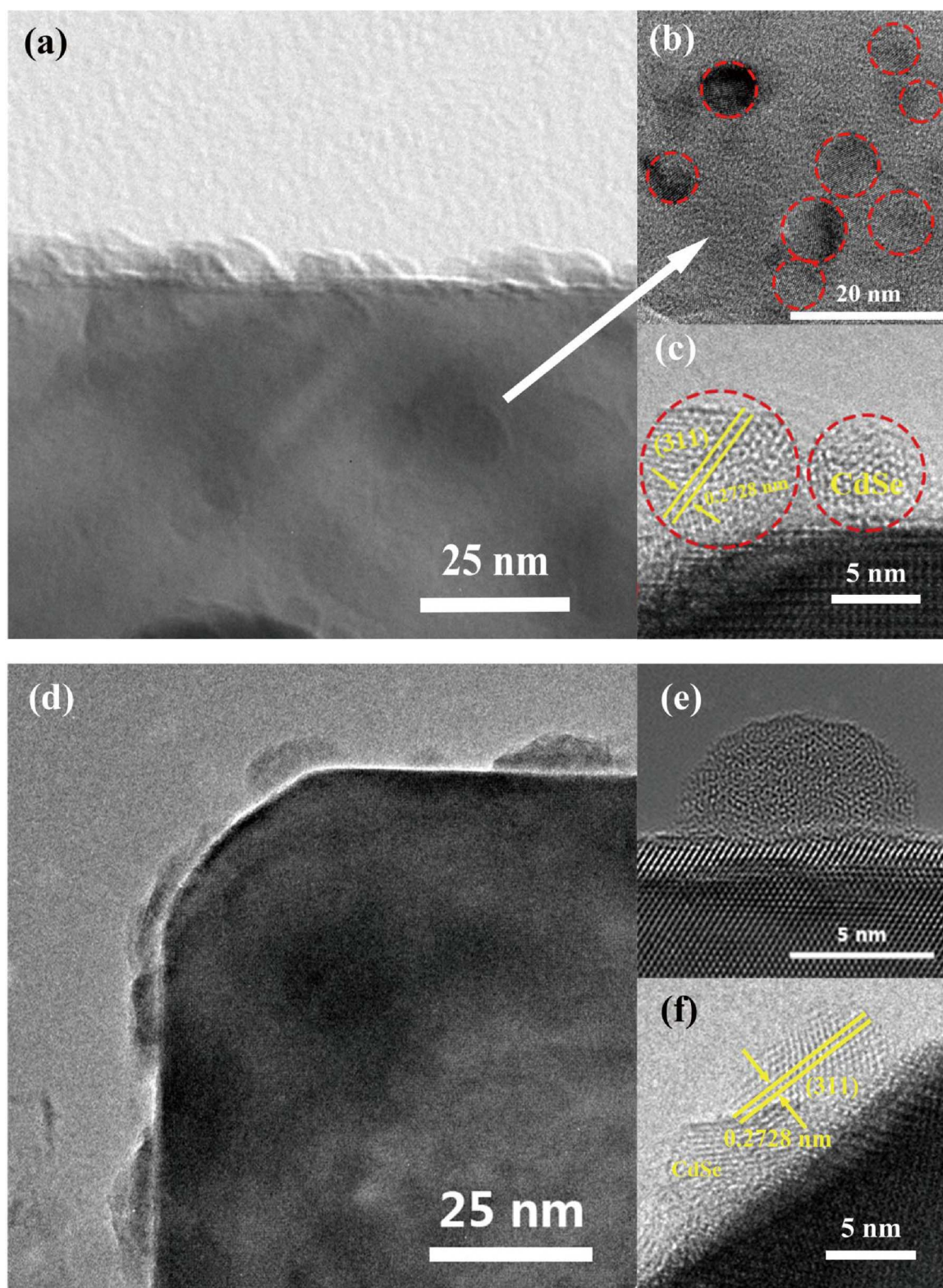


Fig. 7. TEM patterns of BTO-L-7.5 (a–c) and BTO-H-7.5 (d–f).

frequency, band gap, a constant and $n = 2$ or $1/2$ for direct band gap or indirect band gap semiconductors, respectively. As shown in Fig. 11a, it is apparent that there is an approximately 3.19 eV band gap of BTO-H relative to 3.20 eV of BTO-L, respectively. The almost negligible variance demonstrates that the influence of crystal facet exposure on optical absorption of BaTiO₃ can be ruled out. In addition to the absorption edge, the valence band (VB) and conduction band (CB) potentials

of photocatalyst are critical factors of affecting photocatalytic activity. To investigate band structures, valence band XPS was measured with the spectra given in Fig. 11b, revealing that the distances between the Fermi level and the VB maximum are 2.01, 2.08 and 0.74 eV for BTO-H, BTO-L and CS, respectively. Correspondingly, the distances from the Fermi level to the CB minimum can be calculated based on the following equation: [24]

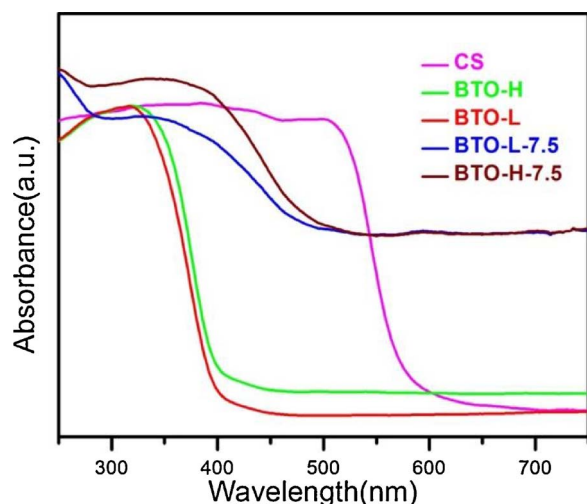


Fig. 8. UV-vis absorption spectra of the as-prepared BTO-L, BTO-H, BTO-L-7.5, BTO-H-7.5 and CS.

Table 2

Specific surface area (BET), electrochemical resistance (EIS), band gap (E_g), photocatalytic activity (PA) and TOF for H_2 generation of prepared catalysts.

Sample	BET (m^2/g)	EIS (Ωcm^2) ^a	E_g (eV)	PA ($mmol g^{-1} h^{-1}$) ^b	TOF (h^{-1})
CdSe	86.27	510.8	2.05	0.053	–
BTO-L	5.67	1291.5	3.20	–	–
BTO-H	5.88	1076.3	3.19	–	–
BTO-L-7.5	10.06	405.8	–	0.327	1.117
BTO-H-7.5	9.89	351.8	–	0.534	1.981

^a The corresponding equivalent circuit of EIS is shown as the inset in Fig. 10b.

^b Catalytic activity is evaluated by hydrogen production rate.

$$E_{CB} = E_g - E_{VB} \quad (4)$$

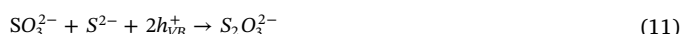
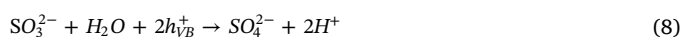
The values of 1.18, 1.12 and 1.31 eV are obtained for BTO-H, BTO-L, and CS, respectively. Mott-Schottky measurements were performed to further detect and confirm potential of the Fermi level. As mentioned in previous literature, [22] the flat band potentials (E_{FB}) of a semiconductor catalyst can be defined by extrapolating the straight portion of the $1/C^2$ against potential plot to the intercept of the tangent to the x axis. As the results given in Fig. 11c and d, it can be seen that the E_{FB} are -0.692 , -0.635 and -0.764 V for BTO-H, BTO-L and CS (versus Ag/AgCl at pH = 6.8), respectively. According to the following equation:

$$E_{(NHE)} = E_{(Ag/AgCl)} + 0.197 \quad (5)$$

$$E_{(RHE)} = E_{(NHE)} + 0.0591pH \quad (6)$$

We can easily calculate the values that equate to -0.093 , -0.036 and -0.165 V of BTO-H, BTO-L and CS versus the normal hydrogen electrode (NHE) at pH = 0, respectively. Additionally, the epitaxial tangents of the Mott-Schottky plots uniformly show positive slope, indicating all of our samples are n-type semiconductors. It is known that the flat potential is equal to the Fermi level (E_F) for n-type semiconductors, whereby the E_F of BTO-H, BTO-L and CS are -0.093 , -0.036 and -0.165 eV, respectively.

Through the above the detection findings, the schematic band structure diagrams of the three semiconductors can be depicted, which is displayed in Fig. 12. They show considerably lower positive potential of CBs compared to the water reduction potential, which illustrates they can act as photocatalysts for water reduction. Moreover, the more negative potential of CdSe compared with both of BTO-L and BTO-H suggests that CdSe QDs work for electron donor and BaTiO₃ act as electron acceptor, resulting in transfer path of photogenerated electron is transferring from CB of CdSe QDs to that of BaTiO₃. On the other hand, owing to the exposure of anisotropic {230} facets on the surface of BaTiO₃ leads to the BTO-H CB more tend to be negative relative to BTO-L, a higher reduction activity can be able to achieve. Holes trapped at CdSe surface atoms can induced anodic corrosion resulting in formation of Se Oxide. Since the valence band of holes is located at $+1.5$ V NHE in aqueous solution, the lattice corrosion of Se ions is inevitable if a free valence band hole is unable to recombine with an electron or to be scavenged by a hole scavenger at the surface. [38] As a consequence, we took this problem into consideration during hydrogen evolution test. An Na₂S + Na₂SO₃ solution was utilized to act as the hole scavenger. Probably, three different routes for scavenging the hole are possible (Eqs. (8), (9) and (11)). The production of S_2^{2-} ions, which act as an optical filter and compete with reduction of protons, is efficiently suppressed by mixing SO_3^{2-} ions. SO_3^{2-} ions yields mainly thiosulfate ions. [39,40]



According to the above results, the schematic illustration of photocatalytic mechanism that enhanced carrier transfer and separation is

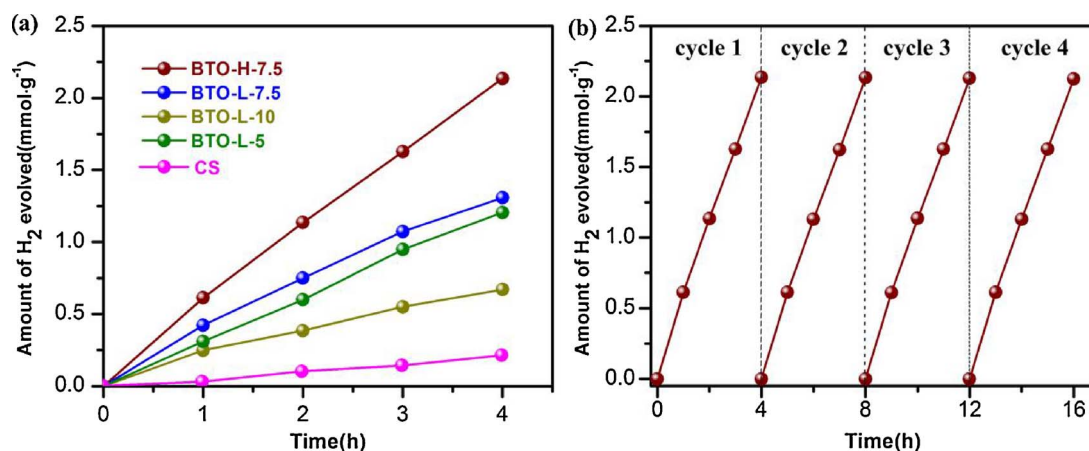


Fig. 9. (a) Photocatalytic water reduction performance of BTO-L-5, BTO-L-7.5, BTO-L-10, BTO-H-7.5 and CS. (b) Cyclic performance of BTO-H-7.5 for hydrogen production under visible light irradiation.

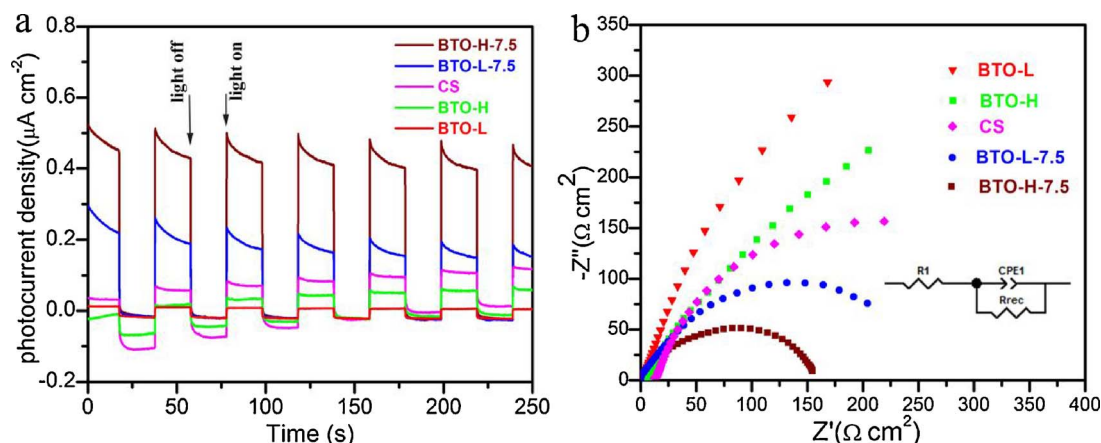


Fig. 10. (a) The transient photocurrent responses of BTO-L, BTO-H, BTO-L-10, BTO-H-10 and CS normalized by light absorption. (b) Electrochemical impedance spectroscopy of BTO-L, BTO-H, BTO-L-10, BTO-H-10 and CS; the inset in figure gives the corresponding equivalent circuit. R_{rec} is the charge-transfer resistance across the electrode/electrolyte interface, R_1 is the solution resistance, CPE_1 is the constant phase component.

shown in Fig. 13.

4. Conclusion

In summary, using a novel chemical bath strategy, CdSe QDs were triumphantly located on isotropic facets of 6-facet cubic BaTiO₃ and anisotropic facets of 30-facet varietal cubic BaTiO₃ indistinguishably. Compared with CdSe QDs sensitized 6-facet cubic BaTiO₃, we found that CdSe QDs sensitized 30-facet BaTiO₃ composite showed enhancement of apparent photocurrent response and superior photocatalytic performance. The enhanced performance should be attributed

intrinsically to the charge migration and separation between CdSe QDs electron donor and BaTiO₃ electron acceptor. In addition, it is the most important point that the closer to CdSe QDs negative potential of anisotropic facets {230} provides electron with a faster transfer channel and result in higher activity of photocatalytic water reduction. The work highlights the impact of morphology in semiconductor photocatalyst systems and illustrates the synergy effect of exposed anisotropic facets in the heterogeneous catalyst system, which should be instructive for the design and preparation of more efficient photocatalyst system.

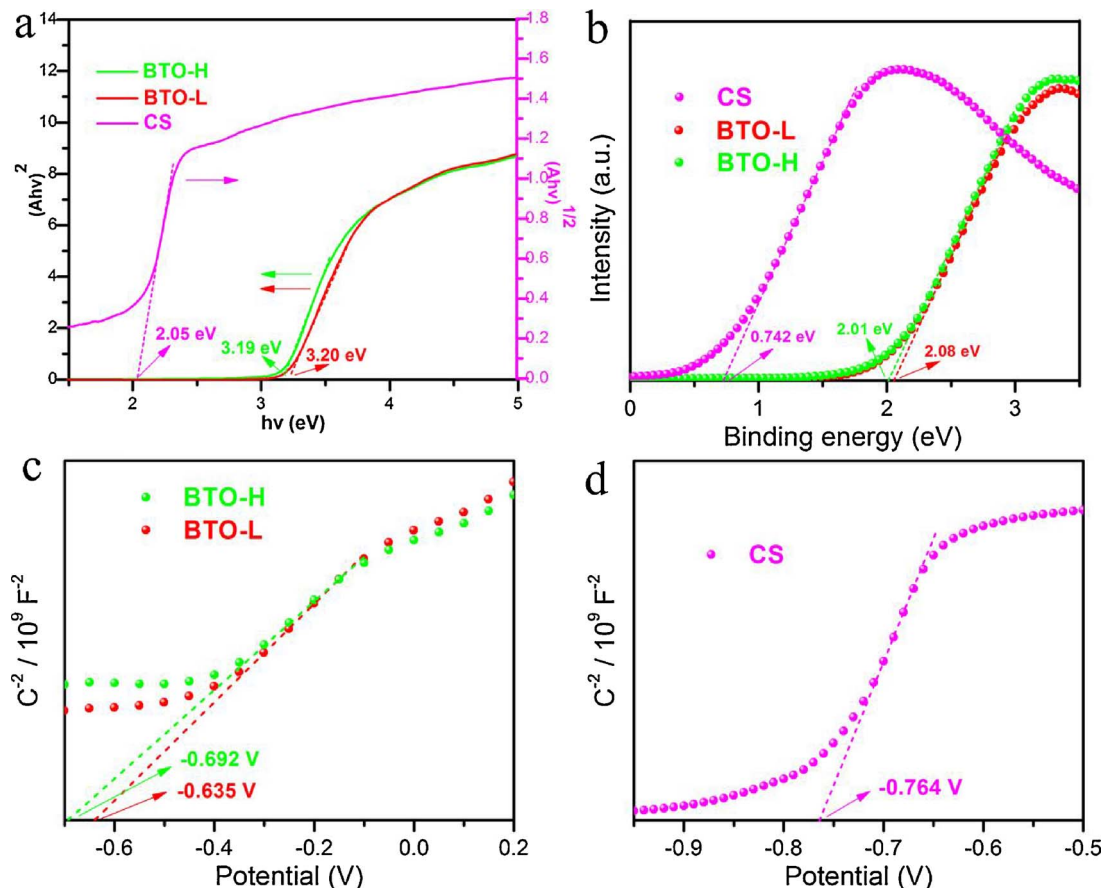


Fig. 11. (a) The band gap energy curves derived from UV-vis DRS spectra, (b) valence band XPS spectra, (c) and (d) Mott-Schottky plots.

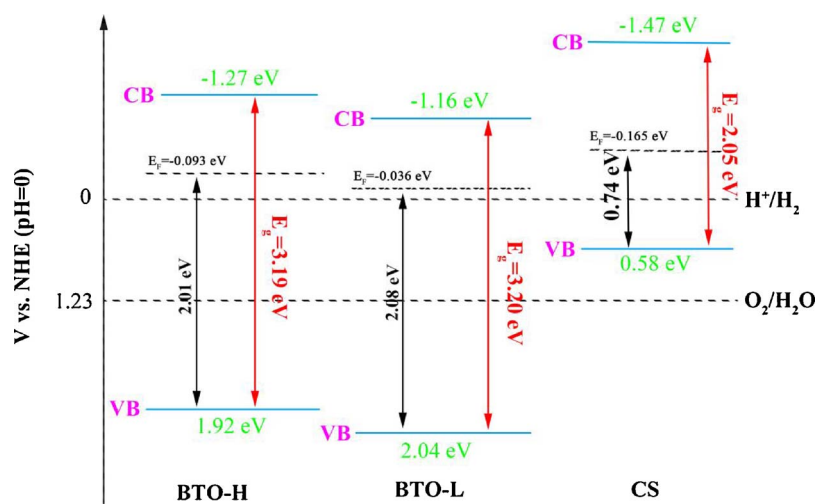
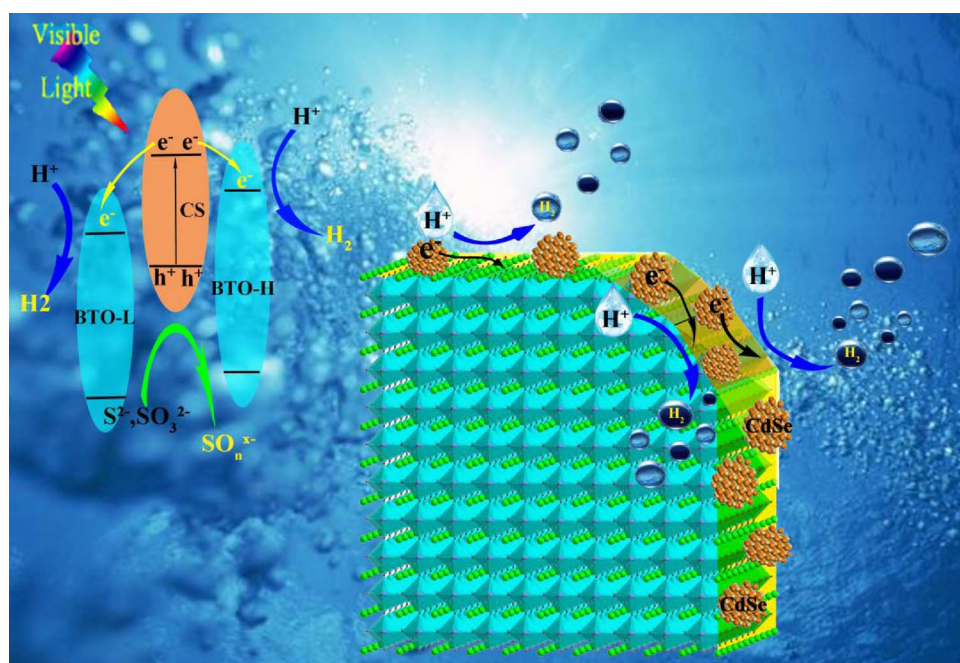


Fig. 12. (e) The proposed band structures of BTO-L, BTO-H and CS.

Fig. 13. Schematic illustration of photocatalytic mechanism for the CdSe quantum dots sensitized BaTiO₃ nanocubes composite structure.

Acknowledgements

We great acknowledge financial support by Science Fund for Distinguished Young Scholars of Hunan Province (2015JJ1026), Program for Shenghua Overseas Talent (90600-903030005; 90600-996010162), the project of Innovation-driven plan in Central South University (2015CX5004) and the National Natural Science Foundation of China (11674398).

References

- [1] D. Kang, T.W. Kim, S.R. Kubota, A.C. Cardiel, H.G. Cha, K.S. Choi, *Chem. Rev.* 115 (2015) 12839–12887.
- [2] W.G. Yang, Y.H. Yu, M.B. Starr, X. Yin, Z.D. Li, A. Kvit, S.F. Wang, P. Zhao, X.D. Wang, *Nano Lett.* 15 (2015) 7574–7580.
- [3] D. Sharma, S. Upadhyay, V.R. Satsangi, R. Shrivastav, U.V. Waghmare, S. Dass, *Appl. Catal. B: Environ.* 189 (2016) 75–85.
- [4] K. Maeda, *ACS Appl. Mater. Inter.* 6 (2014) 2167–2173.
- [5] G. Sreedhar, A. Sivanantham, S. Venkateshwaran, S.K. Panda, M. Eashwar, *J. Mater. Chem. A* 3 (2015) 13476–13482.
- [6] L.C. Mu, Y. Zhao, A.L. Li, S.Y. Wang, Z.L. Wang, J.X. Yang, Y. Wang, T.F. Liu, R.T. Chen, J. Zhu, F. Fan, R. Li, C. Li, *Energy Environ. Sci.* 9 (2016) 2463–2469.
- [7] L.K. Preethi, T. Mathews, M. Nand, S.N. Jha, C.S. Gopinath, S. Dash, *Appl. Catal. B: Environ.* 218 (2017) 9–19.
- [8] W.X. Zou, Y. Shao, Y. Pu, Y.D. Luo, J.F. Sun, K. Ma, C.J. Tang, F. Gao, L. Dong, *Appl. Catal. B: Environ.* 218 (2017) 51–59.
- [9] X.M. Sun, J. Wu, Q.F. Li, Q.Z. Liu, Y.F. Qi, L. You, Z. Ji, P. He, P.F. Sheng, J.X. Ren, W.B. Zhang, J. Lu, J.J. Zhang, *Appl. Catal. B: Environ.* 218 (2017) 80–90.
- [10] X.L. Du, X.L. Wang, Y.H. Li, Y.L. Wang, J.J. Zhao, L.J. Fang, L.R. Zheng, H. Tong, H.G. Yang, *J. Am. Chem. Soc.* 139 (2017) 9402–9405.
- [11] J. Xiao, W.Y. Yang, Q. Li, *Appl. Catal. B: Environ.* 218 (2017) 111–118.
- [12] Y. Zhang, J.R. Chen, L. Hua, S.J. Li, X.X. Zhang, W.C. Sheng, S.S. Cao, *J. Hazard. Mater.* 340 (2017) 309–318.
- [13] J.C. Wang, C.X. Cui, Y. Li, L. Liu, Y.P. Zhang, W. Shi, *J. Hazard. Mater.* 339 (2017) 43–53.
- [14] P.F. Tan, X. Chen, L.D. Wu, Y.Y. Shang, W.W. Liu, J. Pan, X. Xiong, *Appl. Catal. B: Environ.* 202 (2017) 326–334.
- [15] Y.Y. Shang, X. Chen, W.W. Liu, P.F. Tan, H.Y. Chen, L.D. Wu, C. Ma, X. Xiong, *J. Pan, Appl. Catal. B: Environ.* 204 (2017) 78–88.
- [16] Y. Kanigridou, A. Petala, Z. Frontistis, M. Antonopoulou, M. Solakidou, I. Konstantinou, Y. Deligiannakis, D. Mantzavinos, D.I. Kondarides, *J. Chem. Eng.* 318 (2017) 39–49.
- [17] A.A. Ismail, I. Abdelfattah, A. Helal, S.A. Al-Sayari, L. Robben, D.W. Bahnemann, *J. Hazard. Mater.* 307 (2016) 43–54.
- [18] X.B. Wei, C.L. Shao, X.H. Li, N. Lu, K.X. Wang, Z.Y. Zhang, Y.C. Liu, *Nanoscale* 8 (2016) 11034–11043.
- [19] L.X. Zheng, S.C. Han, H. Liu, P.P. Yu, X.S. Fang, *Small* 12 (2016) 1527–1536.
- [20] M. Li, L. Zhang, M. Wu, Y. Du, X. Fan, M. Wang, L. Zhang, Q. Kong, J. Shi, *Nano Energy* 19 (2016) 145–155.
- [21] R.G. Li, F.X. Zhang, D.G. Wang, J.X. Yang, M.R. Li, J. Zhu, X.X. Zhou, H. Han, C. Li,

- Nat. Commun. 4 (2013) 1432.
- [22] J. Pan, G. Liu, G.Q. Lu, H.M. Cheng, Angew. Chem. Int. Ed. 50 (2011) 2133–2137.
- [23] A.Y. Meng, J. Zhang, D.F. Xu, B. Cheng, J.G. Yu, Appl. Catal. B: Environ. 198 (2016) 286–294.
- [24] X.L. Wu, Y.H. Ng, L. Wang, Y. Du, S.X. Dou, Rose Amal, Jason Scott, J. Mater. Chem. A 5 (2017) 8117–8124.
- [25] A.U. Pawar, C.W. Kim, M.J. Kang, Y.S. Kang, Nano Energy 20 (2016) 156–167.
- [26] W.W. Liu, Y.Y. Shang, A.Q. Zhu, P.F. Tan, Y. Liu, L.L. Qiao, D.W. Chu, X. Xiong, J. Pan, J. Mater. Chem. A 5 (2017) 12542–12549.
- [27] B. Wang, S.H. Shen, L.J. Guo, ChemCatChem 8 (2016) 798–804.
- [28] S.R. Vaddipalli, S.R. Sanivarapu, S. Vengatesan, J.B. Lawrence, M. Eashwar, G. Sreedhar, ACS Appl. Mater. Inter. 8 (2016) 23049–23059.
- [29] Y. Chen, C.H. Chuang, Z. Qin, S. Shen, T. Doane, C. Burda, Nature Nanotech. 28 (2017) 084002.
- [30] M.H. Um, H. Kumazawa, J. Mater. Sci. 35 (2000) 1295–1300.
- [31] M. Rastogi, H.S. Kushwaha, R. Vaish, Electron. Mater. Lett. 12 (2016) 281–289.
- [32] T. Tachikawa, S. Yamashita, T. Majima, J. Am. Chem. Soc. 133 (2011) 7197–7204.
- [33] G. Liu, J.C. Yu, G.Q. Lu, H.M. Cheng, J. Am. Chem. Soc. 47 (2011) 6763–6783.
- [34] Q. Xiang, J. Yu, M. Jaroniec, J. Am. Chem. Soc. 134 (2012) 6575–6578.
- [35] S. Keav, A.E. de los Monteros, J. Barbier, D. Duprez, Appl. Catal. B: Environ. 150–151 (2014) 402–410.
- [36] C. Liu, H. Xian, Z. Jiang, L. Wang, J. Zhang, L. Zheng, Y. Tan, X. Li, Appl. Catal. B: Environ. 176–177 (2015) 542–552.
- [37] F. Liu, H. He, C. Zhang, Z. Feng, L. Zheng, Y. Xie, T. Hu, Appl. Catal. B: Environ. 96 (2010) 408–420.
- [38] J. Jasieniak, P. Mulvaney, J. Am. Chem. Soc. 129 (2007) 2841–2848.
- [39] P. Gomathisankar, K. Hachisuka, H. Katsumata, T. Suzuki, K. Funasaka, S. Kaneco, RSC Adv. 3 (2013) 20429.
- [40] P. Gomathisankar, K. Hachisuka, H. Katsumata, T. Suzuki, K. Funasaka, S. Kaneco, ACS Sustain. Chem. Eng. 1 (2013) 982–988.